Complex metallic surface phases in the Al/Cu(111) system: An experimental and computational study

Thomas Duguet, Emilie Gaudry, Thomas Deniozou, Julian Ledieu, Marie-Cécile de Weerd, Thierry Belmonte, Vincent Fournée, Jean-Marie Dubois

Complex metallic surface phases in the Al/Cu(111) system: An experimental and computational study

T. Duguet, E. Gaudry, T. Deniozou, J. Ledieu, M. C. de Weerd, T. Belmonte, J. M. Dubois, and V. Fournée
Institut Jean Lamour, UMR 7198 CNRS–Nancy Université–UPV Metz, Ecole des Mines de Nancy, Parc de Saurupt, CS 14234, 54042 Nancy Cedex, France

(Received 16 October 2008; revised manuscript received 26 June 2009; published 12 November 2009)

The growth of complex intermetallics as surface alloys is investigated by annealing Al thin films deposited on Cu(111) substrate in ultrahigh vacuum. Already at room temperature, the large lattice mismatch between Al and Cu results in interfacial intermixing. Upon annealing, various phases are formed by diffusion depending on the thickness of the Al films and the annealing temperature. The surface structures are characterized by scanning tunneling microscopy, low-energy electron diffraction, and x-ray photoelectron spectroscopy. Three different superlattice phases are identified as well as the complex Hume-Rothery γ-Al_4Cu_9 phase. The epitaxial relationships between the surface phases and the Cu(111) substrate are determined. We further investigate the electronic structure of the γ phase by density functional calculations. Experimental valence bands are compared to calculated density of states and simulated STM images are used to identify possible bulk planes appearing as surface termination.

DOI: 10.1103/PhysRevB.80.205412 PACS number(s): 68.37.Ef, 68.35.Rh, 71.23.Ft, 71.15.Mb

I. INTRODUCTION

Complex metallic alloys (CMAs) represent an emerging field in materials science.[1] They are defined as intermetallic compounds possessing a large unit cell containing a high number of atoms, usually ranging from some tens to a few thousands.[2,3] A structural characteristic of CMAs is the existence of a cluster substructure accounting for most of the atomic positions. These clusters are formed from highly symmetric concentric shells, often presenting icosahedral symmetry, and located on the periodic lattice nodes. Due to their lack of translational symmetry, quasicrystals are considered as a special case of CMAs, for which the clusters are quasiperiodically distributed in space.[4] Interesting physical properties may emerge from these materials as the cluster substructure defines an additional (shorter) physical length scale compared to the lattice dimensions that may significantly influence their properties. Some properties of CMAs are indeed different compared to usual metallic alloys, like their transport properties for example. The resistivity values for Al-based CMAs are several orders of magnitude larger than for pure Al, and the temperature coefficient of the resistivity is negative.[5] Surface properties of CMAs, such as friction and adhesion or wetting, are also different.[6–10] A characteristic feature of their electronic structure is the existence of a reduced density of states (DOS) in the vicinity of the Fermi level. The origin of this pseudogap has been interpreted as a Hume-Rothery effect combined with *sp-d* hybridization.[11,12]

So far, only a limited number of CMAs can be grown as large single grains as required for surface studies. Here, we explore the possibility to grow CMAs as surface alloys. The Al-Cu system was selected as a case study, because the phase diagram contains several structurally complex compounds, such as the orthorhombic ζ-Al_3Cu_4 (Refs. 13–15) (83.3 atoms per unit cell) and the cubic γ-Al_4Cu_9 (Ref. 16) (52 atoms per unit cell) phases. Both of these alloys have been identified as Hume-Rothery compounds. Indeed, elemental constituents have similar metallic radii ($r_{Al}/r_{Cu}=1.12$) and a small electronegativity difference, two of the Hume-Rothery criteria. The third criterion imposes the valence electron concentration n to be such that the radius of the free-electron Fermi sphere $k_F=(3\pi^2 n)^{1/3}$ coincides with the most prominent Brillouin zone (also called Jones zone) constructed from Bragg planes with strong scattering potential. In the case of the γ-Al_4Cu_9 phase, the matching condition $k_F \approx K_p/2$ (K_p is the magnitude of the reciprocal lattice vector) is satisfied by the {330} and {411} zone planes. A recent analysis of this system by Asahi *et al.*[17] has rigorously demonstrated that the scattering of the electron wave functions by this particular set of planes is indeed responsible for the formation of a sizeable pseudogap at E_F and contributes to the alloy stability.

In order to form such complex metallic phases as surface alloys, we grow Al thin films on Cu(111) at room temperature in ultrahigh vacuum. Then we study the phase transformations occurring at the surface upon annealing. The growth of Al thin films on Cu(111) system has not been reported so far. However, it is found that Cu grows in a layer-by-layer mode on Al(111) and that interfacial diffusion already occurs in the submonolayer regime.[18] Intermixing is related to strain relaxation induced by the 12% lattice mismatch ($a_{Al}=4.05$ Å and $a_{Cu}=3.61$ Å). Above 2 monolayers (MLs), Cu grows epitaxially and the Cu bulk lattice parameter is recovered at 10 ML.[18,19] Other related studies have focused on Al/Cu/Fe multilayers and have determined the phase transformations occurring during *in situ* annealing by synchrotron radiation diffraction.[20,21] It was found that Al and Cu layers intermix first and form the following sequence of phases with increasing annealing temperature: $Al+Cu \rightarrow \beta$-$AlCu_3 \rightarrow \beta'$-$Al_xCu \rightarrow \theta$-$Al_2Cu \rightarrow \eta_2$-AlCu. The formation of Al_2Cu, Al_4Cu_9, $AlCu_3$, and Al_xCu has also been reported in similar studies.[22–25] In particular, Jiang *et al.*[24] have shown that the formation of θ-Al_2Cu and γ-Al_4Cu_9 is controlled by interfacial and grain boundary diffusion. Activation energies of about 0.8 eV have been determined for the

formation of these two phases. These values obtained for multilayers are much smaller than the corresponding energies obtained for bulk samples (1.2 eV).[24] Thus, many intermetallics, including structurally complex phases, can be formed by reactive diffusion in the Al-Cu system and their activation energy is significantly lowered in thin films. This supports our choice of the Al-Cu system to study the formation of CMA as surface alloys.

The paper is organized as follows. Section II describes the experimental results. We first give experimental details and describe the growth of Al thin films on Cu(111) at room temperature. Then we identify the surface structures formed upon annealing the films using scanning tunnelling microscopy (STM), low-energy electron diffraction (LEED), and x-ray photoemission spectroscopy (XPS). We also investigate the electronic structure of the γ-Al_4Cu_9 surface alloy by ultraviolet photoelectron spectroscopy (UPS). Section III deals with the electronic structure of this particular alloy investigated by density functional calculations. The calculated DOS and simulated STM images are used to interpret the experimental results. A conclusion is provided in Sec. IV.

II. EXPERIMENTAL RESULTS

A. Experimental details

Experiments are performed in an ultrahigh vacuum multichamber system with a base pressure of 5.10^{-9} Pa. The Cu(111) surface is prepared by sputtering (Ar^+, 2 keV) and annealing (900 K) cycles. The cleanliness of the surface is controlled by XPS. Thin films are deposited using a cold lip Al source (purity 5*N*) and the pressure is kept below 2×10^{-8} Pa during deposition. The flux is calibrated by analysis of STM images at submonolayer coverage. The coverages given below must be considered as estimations, because intermixing in the submonolayer regime may cause errors in the flux calibration. Within this limitation, the deposition rate has been kept constant at a value of 0.05 ML s^{-1} for all experiments and the coverage investigated ranged from 0.6 to 35 ML.

The film growth is monitored as a function of the coverage (θ) and annealing temperature using STM (Omicron VT-STM) and LEED. We used fixed tunnelling conditions (+1.5 V, 0.2 nA). The valence bands are measured by UPS using a He I source (21.2 eV) and a SPHERA hemispherical analyzer. The near-surface composition is determined by core-level XPS with Mg $K\alpha$ (1253.6 eV) radiation. The emission angle between the surface normal and the electron analyzer is set to 45°. The LEED patterns are analyzed using the LEEDPAT v.2.1 software.[26] Annealing is achieved either by electron bombardment (during substrate preparation and *in situ* LEED experiments) or by resistive heating (during *in situ* STM experiments). The temperatures mentioned in the following have been calibrated using a thermocouple attached to an empty tantalum plate. The real surface temperature is expected to be slightly lower than that of the sample plate.

In addition, two polycrystalline samples with nominal composition Al_4Cu_9 and Al_2Cu have been prepared by arc-melting and sintering. These two bulk samples have been characterized by powder x-ray diffraction and identified as the cubic phase γ-Al_4Cu_9 (space group $P\bar{4}3m$, a=8.71 Å)[16] and the tetragonal phase θ-Al_2Cu (space group $I4/mcm$, a=6.06 Å, and c=4.87 Å).[27] A clean surface was obtained after repeated cycles of sputtering (Ar^+, 2 keV) and annealing (900 K) in UHV. Preferential sputtering of Al is likely to produce an Al-depleted surface. Therefore, we have checked that the bulk composition can be restored in the near surface region after annealing at 900 K. We found values of $Al_{67\pm5}Cu_{33\pm5}$ and $Al_{32\pm5}Cu_{68\pm5}$ for θ-Al_2Cu and γ-Al_4Cu_9, respectively, hence within the stability range of these phases according to the equilibrium phase diagram.

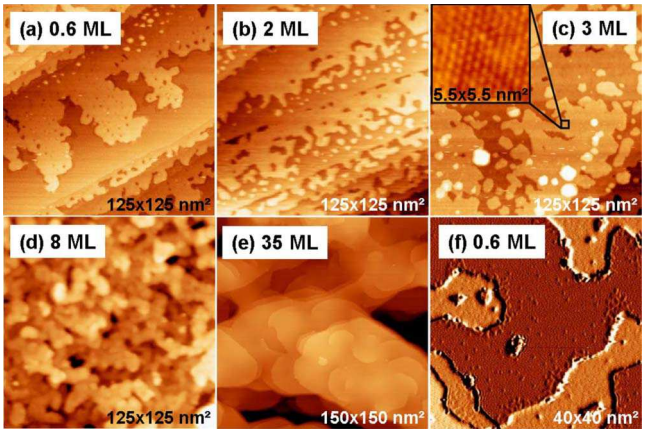

FIG. 1. (Color online) STM images of Al/Cu(111) deposited at room temperature for different film thicknesses (+1.5 V, 0.2 nA).

B. Room temperature deposition

The clean Cu(111) surface exhibits large terraces with a constant step height of about 2.1 Å in agreement with the $d_{(111)}$ interplanar spacing of fcc Cu. The nearest-neighbors distance in the Cu(111) plane deduced from the LEED patterns is equal to 2.55 ± 0.10 Å. Reciprocal space distances reported in the following are calibrated using diffraction patterns of the clean Cu(111) surface.

Figure 1 shows a sequence of STM images with increasing Al coverage. Two-dimensional (2D) growth is observed up to 3 ML with a preferential attachment of adatoms at step edges, although few isolated islands are visible in Figs. 1(a) and 1(b). At 3 ML, atomically resolved STM images [inset of Fig. 1(c)] reveal an hexagonal unit mesh with lattice parameter equal to 5.2 ± 0.1 Å, suggesting a $p(2\times2)$ superstructure on the (111) surface. For higher coverages, substrate steps are no more visible and islands nucleate on terraces with a 3D character [Figs. 1(c) and 1(d)]. These three-dimensional (3D) islands coalesce for coverages larger than 16 ML. The Al film contains a high density of dislocations as can be seen at 35 ML [Fig. 1(e)]. These must be screw dislocations, as their Burger vector is parallel to the dislocation line, perpendicular to the surface plane. The faceted character of the islands in the submonolayer regime [Fig. 1(f)] suggests that the film grows epitaxially on Cu(111), with facets running parallel to low-index directions of the substrate ($\langle\bar{1}10\rangle$ and $\langle10\bar{1}\rangle$). However, intermixing at

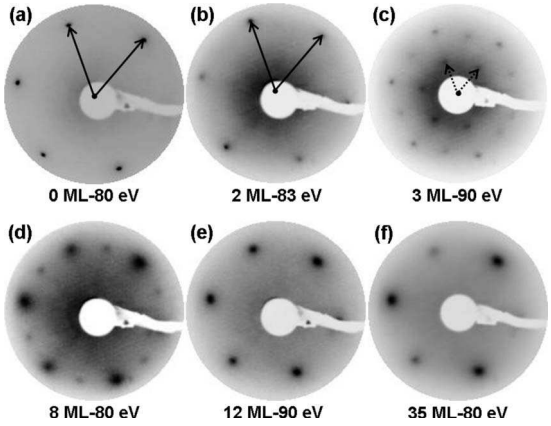

FIG. 2. LEED patterns of Al/Cu(111) deposited at room temperature for different film thicknesses: (a) clean Cu(111) substrate, (b) 2 ML, (c) 3 ML showing a $p(2\times2)$ pattern, (d) 8 ML showing a faint $p(2\times2)$ pattern and large Al(1×1) spots, (e) and (f) 12 ML and 35 ML of Al, respectively, with bulk Al(111) lattice parameter.

submonolayer coverage is expected considering the large lattice mismatch between Al and Cu. Indeed, a pure epitaxial Al film on Cu(111) would be highly strained. Intermixing is actually suggested by the presence of defects observed mainly at step edges but also on terraces as seen in the image shown in Fig. 1(f).

The LEED patterns recorded at different coverages are shown in Fig. 2. For $\theta<3$ ML, a (1×1) pattern is observed with a lattice parameter close to that of the substrate ($a_{\mathrm{Cu}(111)}=2.55$ Å). The background intensity increases upon Al deposition. At 3 ML, additional spots appear in the LEED pattern defining a $p(2\times2)$ superstructure based on a (111) unit mesh with a lattice parameter of 2.65 ± 0.1 Å, i.e., intermediate between that of pure Al and Cu metals. This is consistent with the STM image recorded at 3 ML coverage shown in Fig. 1(c). The $p(2\times2)$ superstructure gradually disappears between 8 and 12 ML and a (1×1) pattern is recovered above 12 ML with a lattice parameter close to that of Al(111) ($a_{\mathrm{Al}(111)}=2.86$ Å).

The STM and LEED data are consistent with the following growth scenario. First the film grows in an imperfect layer-by-layer mode on Cu(111) up to 3 ML. It has a (111) structure with a lattice parameter close to that of the substrate. The interfacial strain induced by the 12% misfit may be relaxed through intermixing, as suggested by STM images already in the submonolayer regime. Thus the film probably contains some Cu at this stage and should correspond to an α-(Al) solid solution. The Cu content of the film could not be estimated, because the thickness probed by XPS within our experimental conditions is larger than 3 ML and thus the Cu substrate necessarily contributes to the photoelectron intensity. At 3 ML, the surface shows a $p(2\times2)$ superstructure. Then for $3\ \mathrm{ML}<\theta<8$ ML, 3D growth of Al(111) (with $a=2.80\pm0.1$ Å $\sim a_{\mathrm{Al}(111)}$) occurs on the $p(2\times2)$ surface. Above some critical coverage estimated to fall in the range $8\ \mathrm{ML}<\theta_c<12$ ML, only Al(111) spots remain. The critical coverage θ_c is the nominal thickness of the Al buffer layer needed to grow bulk-like Al(111) thin film on a Cu(111) substrate at room temperature. Note that for Cu deposited on Al(111), a similar film thickness of about 10 ML was required to recover the bulk Cu lattice parameter.

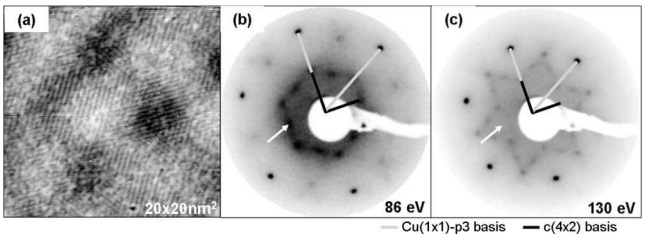

FIG. 3. (a) STM image obtained after annealing 8 ML of Al on Cu(111) at 510 K (+1.5 V, 0.2 nA). (b) and (c) Corresponding LEED patterns for two different beam energies. The basis vectors of the primitive lattice and of the superstructure are indicated. The arrow points toward diffraction spots exhibiting a strong energy dependence.

C. Annealing Al/Cu(111)

Films of various thicknesses have been annealed using the same thermal treatment. Samples are heated up to 510 K within 10 min, maintained at this temperature for another 10 min and cooled down to room temperature. Figure 3 presents the typical surface structure obtained after annealing Al thin films for coverages ranging between 8 and 12 ML. The STM image in Fig. 3(a) shows alternating bright and dark contrast regions indicating a rumpled surface with hills and valley. The length scale of the contrast modulation is smaller than 10 nm. This rumpling might be related to subsurface misfit dislocations. Indeed it is known that interfacial strain induced by the lattice mismatched in heteroepitaxial systems can be relaxed by the formation of misfit dislocations at the layer-substrate interface.[28] These subsurface dislocations can give rise to pronounced surface deformation, similar to what we observe by STM.

The surface atomic structure could not be resolved by STM. Figure 3(a) shows that it contains a lot of disorder. Nevertheless, atomic rows can be distinguished, superimposed on the undulation pattern. Three possible orientations of the rows are observed, rotated by 120° from each other. The average distance between adjacent rows is measured both in direct space and in the fast-Fourier transform of the image and takes value of 4.6 ± 0.3 Å. This information alone is not enough to identify the surface structure.

Figures 3(b) and 3(c) shows the corresponding LEED patterns for two different energies. The most intense diffraction spots define a hexagonal pattern corresponding to a (111) structure with nearest-neighbors distance equal to 2.60 ± 0.1 Å, i.e., close to that expected for fcc Cu. All other spots can be completely explained in terms of three rotational domains of a rectangular $c(4\times2)$ superstructure. The real space and the corresponding diffraction pattern including the three rotational domains are sketched in Fig. 4. Note that some of the superstructure spots exhibit a strong energy dependence. The positions of these spots are indicated by an arrow in the two LEED patterns shown in Figs. 3(b) and 3(c).

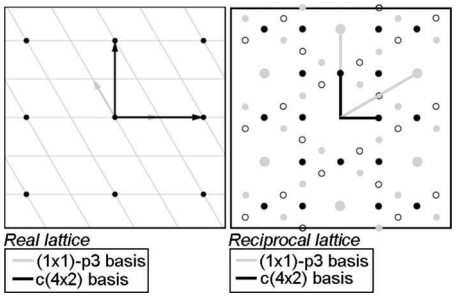

FIG. 4. (a) Sketch of the real space $c(4\times2)$ superstructure. (b) Calculated LEED pattern for three rotational domains of the $c(4\times2)$ superstructure. The arrow points toward diffraction spots exhibiting a strong energy dependence as in shown in Fig. 3.

The surface composition has been estimated from the area under the Al 2s and Cu 3s XPS core-level spectra, weighted by the corresponding photoionization cross-sections. It does not necessarily reflect the composition of the top surface plane, because the chemical composition is probably not homogeneous along the surface normal. We estimate below the information depth (ID) probed in XPS, which is defined as the sample thickness from which a specified percentage of the detected signal originates.[29] It is given by the analytical expression $\mathrm{ID}=-\lambda_i \cos\phi \ln[1-P/100]$, where λ_i is the inelastic mean free path of the photoelectrons, ϕ is the emission angle (45° in our case), and P is a selected percentage. The inelastic mean free path λ_i for Al 2*s* or Cu 3*s* photoelectrons can be approximated using the analytical formula proposed by Tanuma *et al.*[30] This requires the knowledge of the density of the solid, which we assume to be intermediate between that of Al and Cu. This leads to values of λ_i comprised between 25.6 and 31.1 Å. It follows that 90% (95%) of the signal originates from a thickness of 41–50 Å (54–66 Å). Taking an interlayer distance of 2.1 Å, this corresponds to an information depth of about 20–25 ML (25–30 ML). The composition of this near surface region after annealing 8 ML of Al on Cu(111) is estimated at $Al_{22\pm5}Cu_{78\pm5}$ using this method, suggesting that the $c(4\times2)$ superstructure form on a Cu-rich phase. The Al content is close to the maximum solubility of Al in α-(Cu) solid solution according to the equilibrium phase diagram (~18 at. % Al). We also note that extended solid solutions have been reported in Al-Cu thin films produced by co-sputtering.[31] Thus, both LEED and XPS suggest that the $c(4\times2)$ superstructure form on a α-(Cu) solid solution.

Figure 5 presents the typical surface structure obtained after annealing a 35 ML thick Al film under the same conditions as mentioned above. The STM image in Fig. 5(a) shows a terrace and step morphology. Within a single terrace, several crystalline domains coexist, separated by grain boundaries. The surface mesh is the same for each domain, but occurs according to different orientations relative to the substrate. The dimensions of the rectangular unit cell deduced from STM images are $a=8.7\pm0.3$ Å and $b=12.3\pm0.4$ Å. These dimensions are close to those expected for the surface unit cell of (110) planes of the γ-Al_4Cu_9 phase.[27] Two high-resolution STM images of the surface are shown in Figs. 11(c) and 11(f). These two images

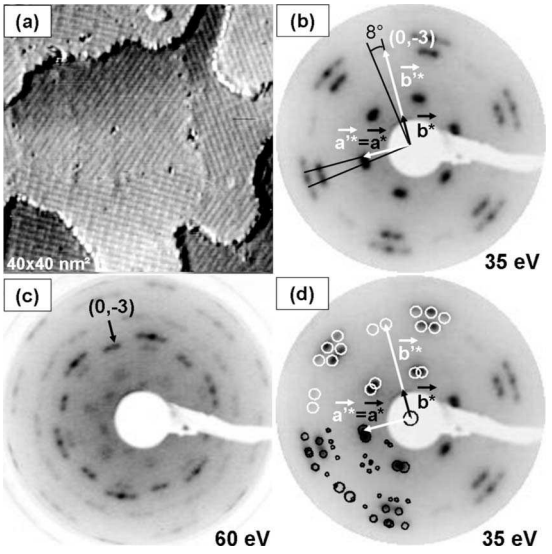

FIG. 5. (a) STM image of the γ-Al_4Cu_9 phase obtained by annealing 35 ML of Al/Cu(111) at 510 K (+1.5 V, 0.2 nA). Corresponding LEED patterns at 35 eV (b) and 60 eV (c). The basis vectors are indicated both for γ-(110) surface mesh (a^* and b^*) and for the reduced surface mesh (a'^* and b'^*) (see text). (d) The scaled reciprocal lattice of the reduced mesh (a'^* and b'^*) (white circles shown in the top part) and the scaled reciprocal lattice weighted by the structure factors of the γ-(110) mesh (a^* and b^*) (black circles shown at the bottom part) are superimposed on the 35 eV LEED pattern. The $(0,-3)$ spots in the (a^* and b^*) are indicated in (b) and (c).

are characteristic of the two different types of STM contrast observed at the surface. The dimensions of the unit cell are the same for both types of terraces, but the contrast inside the unit cell appears different. The type of STM contrast shown in Fig. 11(c) is the most commonly observed one. This suggests that two different terminations appear at the surface. This point will be further discussed in Sec. III. We note also that some disorder can be observed in these STM images, where brightest protrusions can shift along the b direction to larger [top of Fig. 11(c)] or shorter [bottom of Fig. 11(f)] distances. A unique step height of about 2 Å is measured by STM, consistent with the bulk interlayer spacing. However, this does not mean that adjacent terraces separated by a step are necessarily consecutive layers of the bulk model, because island boundaries can coincide with domains boundaries. An evidence for this is the occurrence of different rotational domains observed on adjacent terraces in some of the images. It is even possible that the two types of terminations coexist with the same orientation with respect to the substrate and within a single terrace.

Figure 5(b) shows the LEED pattern of the film recorded at 35 eV while the pattern shown in Fig. 5(c) has been recorded at 60 eV. It can be explained in terms of two sets of three rotational domains of a rectangular mesh, the two sets being rotated by 8° from each other. The basis vectors of the surface mesh are indicated in the figure. The dimensions of the rectangular unit cell deduced from the LEED are $a'=a=8.4\pm0.3$ Å and $b'=b/3=4.1\pm0.3$ Å. Equivalently, the LEED pattern is consistent with two sets of three rota-

tional domains of γ-(110) with (a,b) lattice parameter, with only $(m,3n)$ spots having appreciable intensity, with (m,n) integers. In Fig. 5(d), we overlap the scaled reciprocal lattices of the two sets of threefold rotational domains of the reduced mesh (a'^* and b'^*) onto the experimental LEED pattern, without taking into account the influence of the structure factors on the diffracted intensities. In addition, we also show in Fig. 5(d) the overlapping of the scaled reciprocal lattices (a^* and b^*), weighted by the structure factors, for two sets of three rotational domains of the (110) surface of the γ phase. The spectral weight is represented by the size of the spots in Fig. 5(c). It is obvious that along b^*, only the $(m,3n)$ spots of the γ phase has appreciable intensity. The (0,3) spots have a momentum transfer of 3.17 Å^{-1}, in reasonable agreement with that of the strong $(3\bar{3}0)$ reflection (3.062 Å^{-1}) of the bulk γ-Al_4Cu_9 phase as determined by x-ray diffraction.[16] The fact that weak reflections of the γ-Al_4Cu_9 phase are not observed in the LEED patterns indicates the presence of some disorder compared to the perfect bulk truncation of the γ phase. We note that the diffraction pattern of this surface alloy is consistent with that reported by Bielmann *et al.* for γ-Al_4Cu_9 thin film with (110) surface orientation grown on a quasicrystalline substrate.[32]

The composition in the near surface region has been determined by XPS after annealing either 16 or 35 ML of Al on Cu(111). In both cases, the composition was $Al_{27\pm5}Cu_{73\pm5}$, i.e., close to the composition range of the γ-Al_4Cu_9 phase although slightly Cu-enriched. We stress again that this composition is only indicative because the composition is probably not homogeneous over the thickness probed by XPS. Nevertheless, the combined STM, LEED, and XPS experiments strongly support the formation of the γ phase with (110) surface orientation.

The diffraction patterns of substrate and film show that the domains of the cubic γ-phase are rotated by $\pm4°$ (±1) with respect to the Cu(111) substrate. This $\pm4°$ misorientation between the cubic lattice and the (111) substrate probably originates from an epitaxial relationship similar to the Kurdjomov-Sachs (KS) relationship.[33,34] In the ideal KS case used to describe the epitaxial relationship of fcc(111)/bcc(110) interfaces, the two equivalent domains occur at $\pm5.26°$. It corresponds to a situation where the densely packed atomic rows ($[1\bar{1}0]$) in the fcc (111) plane are parallel to one of the densely packed rows in the bcc (110) plane ($[\bar{1}11]$ or $[1\bar{1}1]$).

Formation of the γ phase was observed upon annealing Al films of thickness comprised between 16 and 35 ML on Cu(111). We mention that we have frequently observed the coexistence of the $c(4\times2)$ superstructure and the γ phase, especially for an intermediate coverage as seen in Fig. 6 for 8 and 16 ML. In these images, the γ phase appears with a darker contrast than the $c(4\times2)$. We note that the fractional area of the γ phase increases with increasing film thickness.

We did not find any evidence for the formation of other stable phases, like those lying on the Al-rich side of the phase diagram, at least within our experimental conditions. Annealing Al films of similar thickness at higher temperature (640 K instead of 510 K) or annealing very thin film (0.6 ML) at 510 K invariably result in the surface structure shown

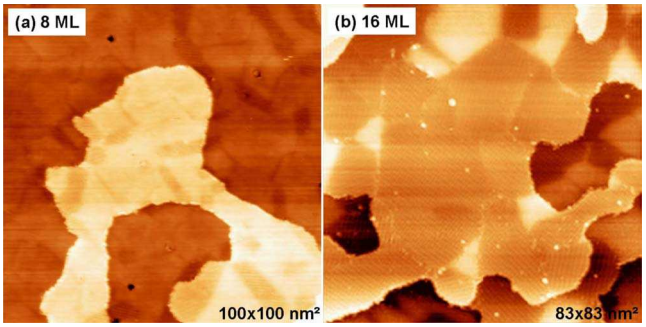

FIG. 6. (Color online) STM images for 8 ML (a) and 16 ML (b) of Al/Cu(111) annealed at 510 K for 5 min. Images recorded at +1.5 V, 0.2 nA.

in Fig. 7. Both atomically resolved STM images and LEED patterns are consistent with a $(\sqrt{3}\times\sqrt{3})R30°$ superstructure on a hexagonal substrate. The size of the overlayer unit cell is 4.30 ± 0.10 Å, close to $(\sqrt{3}/\sqrt{2})\times d_{111}(\mathrm{Cu})=4.42$ Å. The growth of a similar superstructure was already reported on an α-(Cu) solid solution containing less than 9 at.% of Al in Cu.[35,36] This suggests that the Cu diffusion into the Al film is too fast at this temperature, resulting in the formation of a dilute solid solution α-(Cu).

D. *In situ* annealing

In an attempt to determine the possible formation of other compounds, we have performed an *in situ* LEED study of the film as a function of temperature. Aluminum thin films of various thicknesses have been prepared at room temperature and subsequently annealed in front of the LEED optics. The temperature was increased at an average rate of 1.5 K/min. For Al thin films having a thickness comprised between 3 and 12 ML, the following sequence of phase transformations was observed: $\mathrm{Al}(111)\rightarrow p(2\times2)\rightarrow c(4\times2)\rightarrow\alpha$-(Cu)$(\sqrt{3}\times\sqrt{3})R30°$. For thicker films (16 to 35 ML), the sequence is $\mathrm{Al}(111)\rightarrow p(2\times2)\rightarrow\gamma$-$Al_4Cu_9(110)\rightarrow c(4\times2)\rightarrow\alpha$-(Cu)$(\sqrt{3}\times\sqrt{3})R30°$. No evidence for additional phases could be observed in the LEED patterns. It should be mentioned that the LEED pattern referred to as a $p(2\times2)$ superstructure could be equivalently interpreted as three rotational domains of a (2×1) superstructure. STM data would be required to differentiate between these two possibilities. Table I indicates the temperature range within, which each phase in the diffraction pattern could be identi-

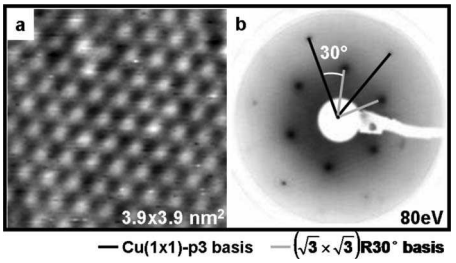

FIG. 7. (a) STM image of the $(\sqrt{3}\times\sqrt{3})R30°$ superlattice phase obtained by annealing 35 ML of Al/Cu(111) at 640 K (Images recorded at +1.5 V, 0.2 nA) and (b) the corresponding LEED pattern.

TABLE I. Temperature ranges (K) of phases observed by *in situ* LEED annealing [min, max].

Coverage (ML)	Temperature range (K)				
	Al(1×1)	α-(Al)-(2×2)	c(4×2)	Al_4Cu_9(110)	α-(Cu)-(1×1)
3	Not observed	[RT-407]	[388–583]	Not observed	≥583
8	[RT-376]	[RT-431]	[431–628]	Not observed	≥628
12	[RT-388]	[RT-444]	[444–615]	≥444	≥615
35	[RT-409]	[≥401]	431	≥438	Not reached

fied for different thicknesses of the deposited films. The temperatures associated to the phase transitions tend to increase in line with film thickness, which is a kinetic effect. During the annealing, both Cu and Al diffusions are activated but a recent study of aluminum-transition-metal bilayers by Buchanan *et al.*[37] has shown that Cu diffusion in Al is much faster than Al diffusion in Cu. Thus surface phase transformation should result from the progressive enrichment of the Al film with Cu diffusing from the substrate. Because the temperature ramp used during the annealing is constant, the appearance of a given phase will be delayed for thicker films, and thus will appear at higher T.

The (2×2) [or (2×1)] superstructure form on a (111) substrate and is observed for all coverages. It is the first surface structure to be formed. Its characteristic diffraction pattern can be detected at room temperature for coverages up to 12 ML and at slightly higher temperature for thicker films, although spots can be very weak. The near surface composition deduced from XPS core-level spectra recorded after room temperature deposition of either 8 or 12 ML of Al on Cu(111) was $Al_{51\pm5}Cu_{49\pm5}$ and $Al_{66\pm5}Cu_{34\pm5}$, respectively. These values are only indicative as the information depth in XPS is much larger than the film thickness as well as the thickness probed by LEED. The lattice parameter of the (111) substrate deduced from LEED patterns is 2.65 ± 0.10 Å, intermediate between that of Al and Cu as already mentioned above. We have also observed that the substrate lattice parameter tends to decrease when the temperature is increased, suggesting a progressive Cu enrichment during the annealing. With increasing temperature, the next surface structure observed is the $c(4\times2)$ superstructure on a Cu-rich (111) substrate, followed by the α-(Cu)$(\sqrt{3}\times\sqrt{3})R30°$, except for thick enough films (>16 ML) for which the γ phase is observed first.

III. ELECTRONIC STRUCTURE CALCULATIONS

In this section, we focus on the electronic structure of the γ-Al_4Cu_9 phase, both in the bulk and at its (110) surface. We first give computational details, and then we compare the calculated density of states with experimental valence bands. Finally we present simulated STM images of possible surface terminations and compare them to experimental STM images.

A. Computational details

The present calculations have been performed within the Density Functional Theory (DFT) framework. Specifically, we have used (i) the Vienna *ab initio* simulation package (VASP) (Ref. 38) to determinate the geometry of the surface by a conjugate gradient minimization of the forces acting on the atoms and (ii) the PWscf code of the Quantum Espresso distribution to determine the bulk electronic structure and to simulate the STM images.[39] Both codes solve the Kohn-Sham equations in a plane wave basis. Our calculations are made within the PW91 approximation for the exchange correlation functional. We use ultrasoft pseudopotential. The calculations are carried out at a fixed cutoff energy of 400 eV, and the irreducible Brillouin zone was sampled by 84 *k*-points for the bulk DOS calculations and by 16 *k*-points for the STM simulations.

The density of states of the bulk Al_4Cu_9 is calculated using the experimental structural model proposed by Dong *et al.*[16,40] The space group of the γ-Al_4Cu_9 phase is $P\bar{4}3m$ and its unit cell contains 52 atoms (a=8.71 Å). The structure model of this phase is shown in Fig. 8 and consist of flat (F,f) and puckered (P,p,P',p') layers separated by about 2 Å and stacked along the [110] direction. The puckered layers contain two additional Al atoms per unit cell compared to flat layers. Using the supercell technique, the (110) surface of Al_4Cu_9 was simulated by repeating a slab of six atomic layers (containing 104 atoms) separated by a 11 Å thick vacuum region in the z direction. We have checked that this thickness of the vacuum region is large enough to avoid any interaction between two consecutive supercells. The lateral lattice parameter was set to the experimental lattice constant of the bulk alloy. The structural model used is then an orthorhombic supercell built on the vectors $\vec{a}$ ($\vec{a}$=[1$\bar{1}$0], a=12.30 Å), $\vec{b}$ ($\vec{b}$=[001], and b=8.70 Å) and

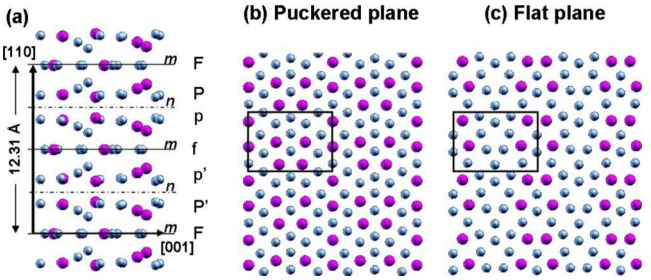

FIG. 8. (Color online) (a) Stacking sequence of flat (F,f) and puckered (P,p,P',p') planes along the [110] direction of the γ-Al_4Cu_9 structure. The atomic structures of puckered and flat planes are shown in (b) and (c), respectively. Large and small dots are for Al and Cu atoms, respectively.

$\vec{c}$ (c=21.3 Å). Three different surface terminations have been considered, corresponding to bulk truncation at different planes along the [110] direction. In the F structural model, the flat layer is selected as the topmost surface layer. In the P_P model, puckered layers of type (P,p') are selected as surface termination while in the $P_{P'}$ model, the surface layer corresponds to a puckered layer of type (P',p) (see labels in Fig. 8). It is necessary to consider these two types of puckered layers since they are not equivalent. In the P_P model, the mean position of Al atoms (Cu atoms resp.) lies at 0.08 Å above (0.04 Å below) the z-mean position of the plane while in the $P_{P'}$ structural model the mean position of Al atoms (Cu atoms resp.) lies at 0.08 Å below (0.04 Å above) the z-mean position of the plane. The peak-to-peak corrugation of both planes is 1.07 Å before relaxation.

A complete relaxation of these supercells remains computationally challenging since the slab must be thick enough such that (i) the model represents a termination of the bulk structure in a realistic way and (ii) the bottom surface has no influence on the studied surface. This is usually treated using a symmetric slab containing at least 6 atomic planes. In our case, this would correspond to a supercell containing 126 atoms (seven atomic layers) for the F model, 162 atoms (nine atomic layers) for the $P_{P'}$ model, and 198 atoms (11 atomic layers) for the P_P model. To reduce computation time and still evaluate reasonably the influence of the relaxation on the simulated STM images, we have adopted a frequent alternative method in which the supercell is asymmetric.[41] This is achieved by allowing the atoms of the first four layers to relax [atoms lying in the surface plane (S), in the subsurface planes S-1, S-2, and S-3] while the positions of atoms lying in the two bottom planes were fixed to mimic the bulk behavior.

B. Calculated density of states and experimental valence bands

Figure 9 shows the total and partial DOS calculated for the bulk γ-Al_4Cu_9. The DOS's are broadened by a Methfessel-Paxton function[42] with a Gaussian width of 0.27 eV. The choice of these criteria allows us to take into account the experimental broadening in photoemission spectra and avoid the loss of signal information (broadening leads to thicker bands which can hide details). The total DOS is consistent with that reported by Mizutani *et al.*[17,43] The Cu d states are the dominant states and form a set of peaks lying between 1.9 and 5.4 eV below the Fermi level, while the Al p, s, and Cu s states extend through all the energy range (occupied and unoccupied states). Here the Fermi energy is taken as the origin for the binding energies. The total DOS presents a minimum in the vicinity of the Fermi level. This is consistent with γ-Al_4Cu_9 being a Hume-Rothery compound.[44–48]

This calculated DOS can be compared with experimental He I valence bands measured by UPS on γ-Al_4Cu_9 thin films. Figure 10(a) also shows the valence bands measured on two polycrystalline samples with structure corresponding to γ-Al_4Cu_9 and θ-Al_2Cu phases. The spectra have been corrected for the background intensity.[49] Due to photoionization

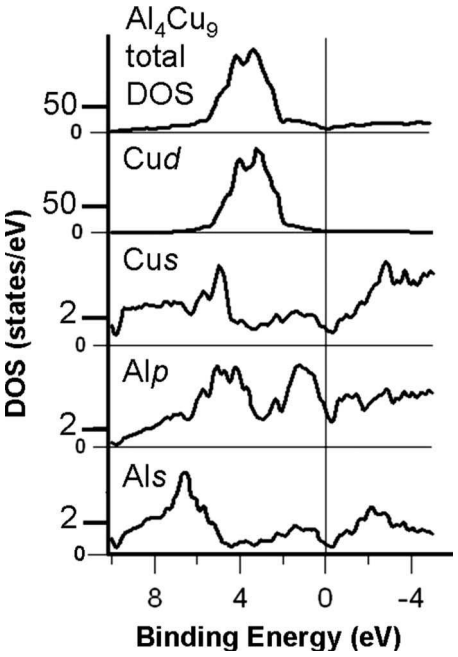

FIG. 9. Total and partial DOS calculated for bulk γ-Al_4Cu_9.

cross-section effects, the spectral intensity is dominated by the Cu d levels in the energy range between 3 and 6 eV below E_F. Compared to pure Cu spectrum (not shown), the d band is shifted by about 2 eV toward higher binding energies upon alloying. This shift is larger for the θ-Al_2Cu phase than for the γ-Al_4Cu_9 phase. Some small discrepancies exist between the experimental and the calculated positions of the Cu d band of the γ-Al_4Cu_9 phase. The experimental position of the Cu d band center is at a binding energy 0.3 ± 0.1 eV (0.6 ± 0.1 eV) larger in the film (respectively, in the bulk polycrystal) than in the calculated DOS. These discrepancies may have different origins such as small stoichiometry differences between γ thin films and the polycrystals or final state effects in photoemission not taken into account in the calculation.

Finally, Fig. 10(b) shows the near Fermi edge structure recorded for θ-Al_2Cu and γ-Al_4Cu_9 bulk polycrystals and for γ thin films. A sharp metallic like Fermi edge is observed for the θ-Al_2Cu sample whereas a clear reduction of the spectral intensity is manifest for the γ-Al_4Cu_9 phase, both in bulk form and in thin films. This is the signature of the pseudogap characteristic of Hume-Rothery compounds and is consistent with the dip at E_F in the calculated total DOS. The similarities between experimental valence bands of the γ phase either in bulk or thin film shapes further support the structural identification of the γ phase as a surface alloy.

C. Simulated STM images

In this last section, we compare experimental STM images recorded on γ thin films with simulated STM images using the model presented above. Images have been simulated using the Tersoff-Hamann model, which approximates the tunnelling current with the LDOS integrated between E_F and E_F+V, where V is the voltage applied between the

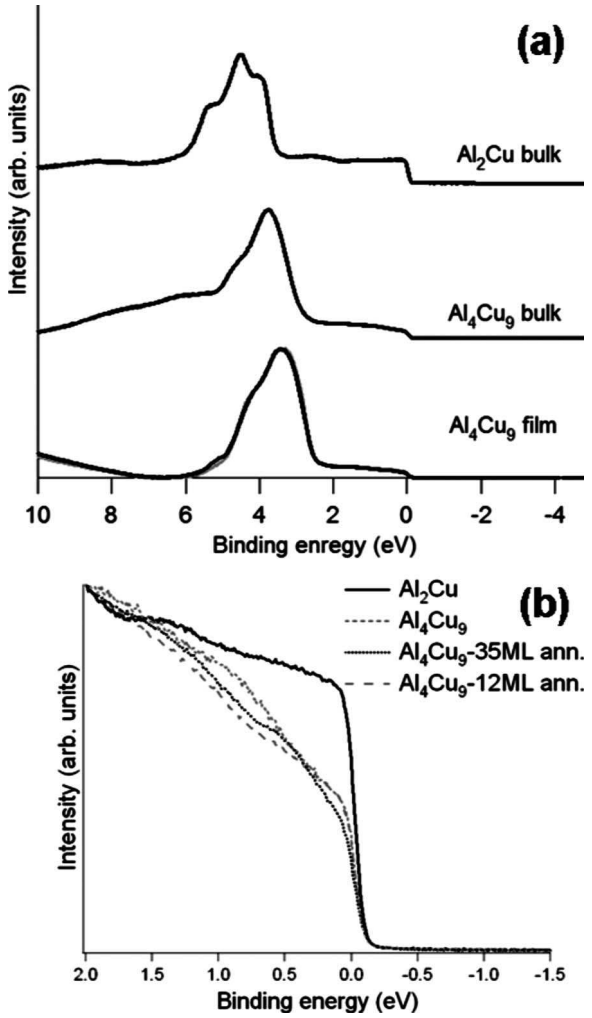

FIG. 10. (a) Normalized UPS spectra recorded on polycrystalline bulk θ-Al_2Cu and γ-Al_4Cu_9 compounds and on γ thin films obtained by annealing 35 ML of Al/Cu(111) at 510 K. (b) Near Fermi edge spectra.

sample and the tip.[50] In this model neither the tip-surface interaction nor the particular shape of the tip are taken into account. The bias V was chosen to match the experimental conditions (V=+1.5 V). Within this approximation, the integrated LDOS $I(V,d,\mathbf{r}_{\|})$ is proportional to the tunnelling current corresponding to V, a tip distance d and lateral position $\mathbf{r}_{\|}$. The images were simulated using a tip-surface distance of 3 Å.

Figure 11 shows the simulated STM images both before and after relaxation using the three different supercell models (P_P, $P_{P'}$, and F) corresponding to the different possible surface terminations of the γ-Al_4Cu_9 (110) surface. First, we note that both types of puckered surface layers (P_P, $P_{P'}$) become flatter upon relaxation. The corrugation (peak-to-peak) of both puckered layers is 1.07 Å before relaxation and reduces to 0.87 Å (0.83 Å) for the P_P layer (respectively, $P_{P'}$ layer) after relaxation. The influence of the relaxation on the calculated STM images is quite drastic in the case of the P_P model [Figs. 11(a) and 11(b)]. Before relaxation [Fig. 11(a)], 4 Al atoms appearing with the brightest contrast form a rectangular unit. Inside this unit, one can recognize a flattened

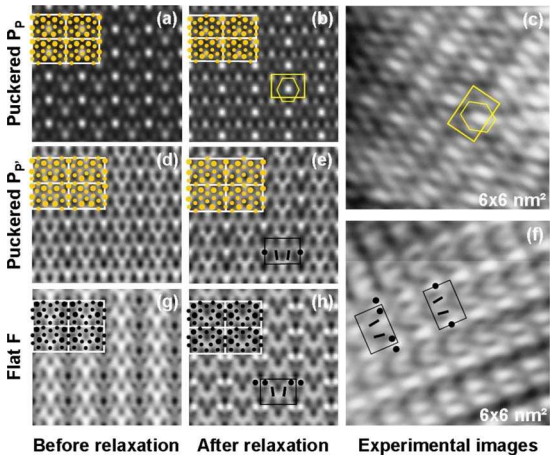

FIG. 11. (Color online) Simulated STM images of the three possible terminations for γ-Al_4Cu_9 (110) surface, both before and after relaxation. Panels (c) and (f) are experimental STM images showing the two different types of terraces. Terrace of the type shown in (c) is the most frequent one. The surface unit cell is superimposed on simulated images. Large and small dots are for Al and Cu atoms, respectively. A schematic of the STM contrast has been added to ease the comparison with experimental images.

hexagonal motif of lower contrast made of 4 Al atoms and 2 Cu atoms, with an additional Cu atom located in the middle of the hexagon. After relaxation [Fig. 11(b)], the Cu atoms decorating the hexagons become the brightest features contributing to the STM contrast. These Cu atoms are located about 0.54 Å above the z-mean position of the plane. A schematic of the STM contrast is superimposed in Fig. 11(b). The same model can be used to interpret the STM contrast observed in the experimental image of the type shown in Fig. 11(c). The rectangular unit is also decorated by a centered hexagonal motif, similar to the simulated image. Thus there is a relatively good agreement between simulated STM images of P_P terminations and terraces of the type shown in Fig. 11(c), although discrepancies exist in terms of the relative intensities. As mentioned earlier, this type of terraces are experimentally the most frequently observed and correspond to atomic planes for which the mean position of Al atoms is above the z-mean position.

STM images calculated for $P_{P'}$ terminations are shown in Figs. 11(d) and 11(e). In this case, the influence of the relaxation is not so drastic. The two brightest features in the unit cell are Al atoms lying about 0.32 Å above the z-mean position of the surface plane. These Al atoms form a rectangular unit mesh with additional contrast forming a v-like shape. A schematic is superimposed in Fig. 11(e). This model is also overlapped on the experimental image shown in Fig. 11(f). The third type of possible surface terminations (F) is considered in Figs. 11(g) and 11(h). Again, significant change is also observed upon relaxation in the simulated images of the flat layers. Here the surface unit cell contains 12 Cu atoms and 4 Al atoms (i.e., two Al atoms less than for puckered layers). After relaxation, one finds that the two brightest features within the unit cell correspond to two Al atoms. Other bright features are mainly due to Cu atoms, forming again a kind of v-like shape decorating the rectan-

gular mesh [Fig. 11(h)]. These simulated STM images of the flat layers are thus characterized by these double bright spots aligned along the $[1\bar{1}0]$ direction, together with the v-like shape as shown in the schematic drawn in Fig. 11(h). This schematic is also overlapped on the experimental image shown in Fig. 11(f). The double bright spots characteristic of F layers is not observed in the experimental images, suggesting that flat layers are not favored as surface terminations. This is in agreement with their lower density compared to $P_{P'}$ and P_P puckered layers.

In conclusion, the comparison between experimental and simulated STM images suggests that both P_P and $P_{P'}$ puckered layers appears as surface terminations whereas F layers do not. However, it is not possible at this stage to unambiguously ascribe a specific termination to either P_P or $P_{P'}$ layer. This is partly due to the presence of surface defects in the STM images and to the fact that artifacts induced by the STM tip cannot be completely ruled out neither.

IV. CONCLUSIONS

We have presented a set of data describing the growth of Al thin films on the Cu(111) surface and the formation of surface alloys induced by annealing. Upon room-temperature deposition and up to 2 ML, the film grows epitaxially with a (111) structure and a lattice parameter close to that of Cu(111). STM images suggest that intermixing does occur at the interface already at room temperature. It is interpreted as a mechanism to relax the strain induced by the large lattice mismatch between Al and Cu atoms. At 3 ML, a $p(2\times2)$ superstructure is observed on a (111) substrate, which could be a solid α-(Al). Upon further deposition, the growth mode becomes 3D. The bulk Al(111) lattice parameter is recovered at $8\ \text{ML} < \theta_c < 12\ \text{ML}$. At high coverages (16 to 35 ML), Al films contain a high density of screw dislocations.

Upon annealing, the Cu content in the film increases and different surface structures appear which can be identified by LEED and STM. For thick enough films (>12 ML), the following sequence of phases is observed at the surface: $\text{Al}(111) \rightarrow p(2\times2) \rightarrow \gamma\text{-Al}_4\text{Cu}_9(110) \rightarrow c(4\times2) \rightarrow \alpha\text{-(Cu)}(\sqrt{3}\times\sqrt{3})\text{R30}^\circ$. We have argued that the $p(2\times2)$ superstructure forms on an Al-rich (111) substrate and that the $c(4\times2)$ superstructure forms on a Cu-rich (111) substrate, most likely α-(Al) and α-(Cu) solid solutions. Three rotational domains of the $c(4\times2)$ superstructure are observed. The γ-phase is the only complex metallic alloy that could be formed using this method. This phase could be stabilized as a surface alloy only when the initial film thickness was larger than 12 ML. Otherwise the $p(2\times2)$ directly transform into the $c(4\times2)$ superstructure. The γ-phase grows with its (110) surface as termination layer. Two sets of three rotational domains have been identified, rotated by $\pm4^\circ$ with respect to the substrate [111] axis.

The electronic structure of the $\gamma\text{-Al}_4\text{Cu}_9$ phase was investigated by *ab initio* calculations and by photoemission spectroscopy. A clear pseudogap is observed in the calculated DOS of the $\gamma\text{-Al}_4\text{Cu}_9$ phase, consistent with the reduction of the intensity of the photoemission spectra near the Fermi edge observed by UPS. Finally, we could interpret high-resolution STM images of the $\gamma\text{-Al}_4\text{Cu}_9$ (110) surface using calculated ones. These simulated STM images have been obtained for the three possible surface terminations along the [110] direction using supercell models. Surface relaxation effects have been taken into account. We found that a reasonable match with the experiments can only be achieved for surfaces terminating at puckered layers. These layers are characterized by a higher-atomic density compared to flat layers.

Finally, we have shown that we could form one CMA as a surface alloy using the method adopted in this work. Although this surface alloy contains defect, the method could be extrapolated to other Al-TM systems presenting CMA phases, with potentially interesting surface properties including chemical reactivity. Such systems could be investigated without the constraint of single crystal growth using this approach. In addition, we have recently reported that the $\gamma\text{-Al}_4\text{Cu}_9$ compound can also be formed on quasicrystalline surfaces with similar epitaxial relationships, the (110) direction of the γ phase being parallel to the fivefold axis of the quasicrystal.[32,51] Consequently we propose that the γ phase could be used as an interfacial layer between an fcc metal substrate and a quasicrystalline coating. The structure and properties of the γ phase are indeed intermediate between a simple metal and a quasicrystal. It is thus reasonable to expect that such an epitaxial interlayer could improve the adhesion of quasicrystalline coatings onto metallic substrates, which currently represents a technological bottleneck.

ACKNOWLEDGMENTS

We are grateful to H. Shin and R. D. Diehl (Physics Department, Pennsylvania State University, University Park, PA 16802, USA) for fruitful discussions about LEED. This work has been supported by the European Network of Excellence on Complex Metallic Alloys (CMA) under Contract No. NMP3-2005-CT-500145 and by the French National Research Agency under Contract No. ANR-05-BLAN-0297-01.

[1] J. M. Dubois, in *Book Series on Complex Metallic Alloys*, edited by E. Belin-Ferré (World Scientific, Singapore, 2008), Vol. 1.
[2] J. M. Dubois, *Useful Quasicrystals* (World Scientific, Singapore, 2005).
[3] K. Urban and M. Feuerbacher, J. Non-Cryst. Solids **334-335**, 143 (2004).
[4] H. Takakura, C. P. Gomez, A. Yamamoto, M. De Boissieu, and A. P. Tsai, Nature Mater. **6**, 58 (2007).
[5] U. Mizutani, J. Phys.: Condens. Matter **10**, 4609 (1998).
[6] E. Belin-Ferré and J. M. Dubois, Int. J. Matter Res. **97**, 985 (2006).
[7] J. M. Dubois, Phys. Scr. **T49A**, 17 (1993).

[8] J.-M. Dubois, P. Brunet, and E. Belin-Ferré, in *Quasicrystals: Current Topics*, edited by E. Belin-Ferré, C. Berger, M. Quiquandon, and A. Sadoc (World Scientific, Singapore, 2000), p. 498.
[9] J. Y. Park, D. F. Ogletree, M. Salmeron, R. A. Ribeiro, P. C. Canfield, C. J. Jenks, and P. A. Thiel, Science **309**, 1354 (2005).
[10] J. Y. Park and P. A. Thiel, J. Phys.: Condens. Matter **20**, 314012 (2008).
[11] U. Mizutani, T. Takeuchi, and H. Sato, Prog. Mater. Sci. **49**, 227 (2004).
[12] G. Trambly de Laissardiere, D. Nguyen-Manh, and D. Mayou, Prog. Mater. Sci. **50**, 679 (2005).
[13] C. Dong, Q. H. Zhang, D. H. Wang, and Y. M. Wang, Eur. Phys. J. B **6**, 25 (1998).
[14] C. Dong, Q. H. Zhang, D. H. Wang, and Y. M. Wang, Micron **31**, 507 (2000).
[15] L. D. Gulay and B. Harbrecht, J. Alloys Compd. **367**, 103 (2004).
[16] C. Dong, Philos. Mag. A **73**, 1519 (1996).
[17] R. Asahi, H. Sato, T. Takeuchi, and U. Mizutani, Phys. Rev. B **71**, 165103 (2005).
[18] H. Asonen, C. J. Barnes, A. Salokatve, and M. Pessa, Surf. Sci. **152-153**, 262 (1985).
[19] C. J. Barnes, H. Asonen, A. Salokatve, and M. Pessa, Surf. Sci. **184**, 163 (1987).
[20] T. Grenet, F. Giroud, J. L. Joulaud, and M. Capitan, Philos. Mag. A **82**, 2909 (2002).
[21] T. Grenet, F. Giroud, K. Loubet, A. Bergman, G. Safran, J. Labar, P. Barna, J. L. Joulaud, and M. Capitan, J. Alloys Compd. **342**, 2 (2002).
[22] M. Cekada, P. Panjan, J. Dolinsek, A. Zalar, Z. Medunic, M. Jaksic, and N. Radic, Thin Solid Films **515**, 7135 (2007).
[23] C.-B. Ene, G. Schmitz, T. Al-Kassab, and R. Kirchheim, Ultramicroscopy **107**, 802 (2007).
[24] H. G. Jiang, J. Y. Dai, H. Y. Tong, B. Z. Ding, Q. H. Song, and Z. Q. Hu, J. Appl. Phys. **74**, 6165 (1993).
[25] J. M. Vandenberg and R. A. Hamm, Thin Solid Films **97**, 313 (1982).
[26] K. Hermann and M. A. Van Hove, http://w3.rz-berlin.mpg.de/~hermann/LEEDpat/.
[27] P. Villars and L. D. Calvert, *Pearson's Handbook of Crystallographic Data for Intermetallic Phases* (ASM International, Materials Park, 1998).
[28] J. Tersoff and F. K. LeGoues, Phys. Rev. Lett. **72**, 3570 (1994).
[29] C. J. Powell and A. Jablonski, Nucl. Instrum. Methods Phys. Res. A **601**, 54 (2009).
[30] S. Tanuma, C. J. Powell, and D. R. Penn, Surf. Interface Anal. **21**, 165 (1994).
[31] F. d'Heurle, C. Alliota, J. Angilello, V. Brusic, J. Dempsey, and D. Irmischer, Vacuum **27**, 321 (1977).
[32] M. Bielmann, A. Barranco, P. Ruffieux, O. Gröning, R. Fasel, R. Widmer, and P. Gröning, Adv. Eng. Mater. **7**, 392 (2005).
[33] G. Kurdjumow and G. Sachs, Z. Phys. **64**, 325 (1930).
[34] E. Bauer and J. H. van der Merwe, Phys. Rev. B **33**, 3657 (1986).
[35] R. J. Baird, D. F. Ogletree, M. A. Van Hove, and G. A. Somorjai, Surf. Sci. **165**, 345 (1986).
[36] M. Yoshitake, S. Bera, and Y. Yamauchi, Surf. Interface Anal. **35**, 824 (2003).
[37] J. D. R. Buchanan, T. P. A. Hase, B. K. Tanner, P. J. Chen, L. Gan, C. J. Powell, and W. F. Egelhoff, Phys. Rev. B **66**, 104427 (2002).
[38] G. Kresse and J. Furthmüller, Phys. Rev. B **54**, 11169 (1996).
[39] S. Baroni, A. Dal Corso, S. De Gironcoli, P. Giannozzi, and C. Cavazzoni, http://www.pwscf.org).
[40] A. J. Bradley, Nature (London) **168**, 661 (1951).
[41] M. Krajčí and J. Hafner, Phys. Rev. B **71**, 054202 (2005).
[42] M. Methfessel and A. T. Paxton, Phys. Rev. B **40**, 3616 (1989).
[43] U. Mizutani, TMS Annual Meeting (unpublished).
[44] E. Belin, Z. Dankhazi, A. Sadoc, J. M. Dubois, and Y. Calvayrac, Europhys. Lett. **26**, 677 (1994).
[45] V. Fournée, E. Belin-Ferré, and J. M. Dubois, J. Phys.: Condens. Matter **10**, 4231 (1998).
[46] V. Fournée, I. Mazin, D. A. Papaconstantopoulos, and E. Belin-Ferré, Philos. Mag. B **79**, 205 (1999).
[47] J. C. Fuggle, E. Källne, L. M. Watson, and D. J. Fabian, Phys. Rev. B **16**, 750 (1977).
[48] G. T. de Laissardière, Z. Dankhazi, E. Belin, A. Sadoc, D. Nguyen Manh, D. Mayou, M. A. Keegan, and D. A. Papaconstantopoulos, Phys. Rev. B **51**, 14035 (1995).
[49] J. Végh, J. Electron Spectrosc. Relat. Phenom. **151**, 159 (2006).
[50] J. Tersoff and D. R. Hamann, Phys. Rev. B **31**, 805 (1985).
[51] T. Duguet, J. Ledieu, J. M. Dubois, and V. Fournée, J. Phys.: Condens. Matter **20**, 314009 (2008).